

Combining Automatic Landmark Detection and Variational Methods for Lung CT Registration

Thomas Polzin¹, Jan Rühaak², René Werner³, Jan Strehlow⁴,
Stefan Heldmann², Heinz Handels⁵, and Jan Modersitzki¹

¹ Institute of Mathematics and Image Computing, University of Lübeck, Germany

² Fraunhofer MEVIS, Project Group Image Registration, Lübeck, Germany

³ Department of Computational Neuroscience, University Medical Center
Hamburg-Eppendorf, Germany

⁴ Fraunhofer MEVIS, Bremen, Germany

⁵ Institute of Medical Informatics, University of Lübeck, Germany

Abstract. This paper proposes a novel method for image registration of lung CT scans. Our approach consists of a procedure for automatically establishing landmark correspondences in lung CT scan pairs and an elaborate variational image registration scheme. The landmark information is incorporated into the registration scheme as pre-registration using the landmark-based Thin-Plate-Spline (TPS) method. The TPS displacement field is improved by an additional minimization of an objective function consisting of a Normalized Gradient Field distance measure, a volume term, and a curvature regularizer. As a special property, landmark correspondences as established by the TPS registration are guaranteed to remain within a user-defined tolerance during the variational registration step.

The new method, called LMP (LandMark Penalty), is applied to the 20 publicly available DIR-Lab data sets and compared to state-of-the-art methods. Particularly on the challenging COPDgene data sets, LMP stands out with an average landmark error of 1.43 mm.

1 Introduction

Registration of lung CT images is a difficult task due to nonlinear motion, volume change and induced shift of intensities. Furthermore, the task is aggravated by the large number of small structures like vessels that move considerably [12]. Possible fields of application for lung image registration range from motion correction during radiotherapy to improved assessment of treatment success or pathogenesis by radiologists [20]. Thus, a lot of attention has been paid to image registration of lung CT scans in recent years; see e.g. [2, 3, 5, 12, 25, 26]. This is also reflected by a large number of participants of the EMPIRE10 challenge [20].

For a comprehensive literature overview on registration of lung CT scans we refer to, e.g., [20]. Here, we focus on some state-of-the-art papers, which provide quantitative registration results for the test data we are working on as well as on papers proposing a methodology that combines feature- and intensity-based registration, which is an approach we propose in this paper as well.

As a first example, the DIR-Lab group published methods for 4D local trajectory modeling (4DLTM) and component phase to phase (CPP) deformable image registration in [2]. Recently, they developed a method based on compressible flow image registration which is combined with a nonlinear filter to obtain the Least median of squares Filtered Compressible flow (LFC) algorithm [3]. Schmidt-Richberg et al. optimized parameters of a nonlinear variational intensity-based registration by evaluation of the registration accuracy during run-time using automatically detected landmark correspondences [26]. Ruhaak et al. additionally included volume regularization and lung segmentations into the variational formulation of the registration problem based on Normalized Gradient Fields image similarity measure and curvature regularization [25]. Recently, Heinrich et al. described a discrete optimization scheme based on Markov random fields, whose vertices build a minimum spanning tree, resulting in low run-times of the registration [12]. In this paper, we follow the lines of Schmidt-Richberg et al. and Ruhaak et al. and augment the variational nonlinear registration approach of Ruhaak et al. by including automatically established landmark correspondences. In contrast to Schmidt-Richberg et al., we directly integrate the landmark information into the energy minimization problem.

For examples on the combination of intensity- and feature-based registration methods see [13–15, 22]. Hellier and Barillot used additional information from sulci in the context of registration of anatomical as well as functional brain images [13]. They employed robust estimators to adapt an optical flow registration. Johnson and Christensen proposed a consistent combined landmark and intensity based registration [14]. Their results with adaptations of Thin-Plate-Spline registrations seem very promising, but unfortunately the evaluation was only performed on two-dimensional data and the computational demand is very high and not easily accomplishable for 3D data. The focus of Kybic and Unser was on efficient registration based on B-spline deformation models as well as B-spline image interpolation [15]. Furthermore, the integration of expert hints was possible by modelling landmark distances as potential energy of springs. And finally and closest to our approach, Papademetris et al. used a weighted functional that consists of intensity and feature components [22]. However, none of these papers on hybrid intensity- and feature-based registration is tackling the problem of registration of pulmonary images and only Hellier and Barillot used automatically detected features [13]. Furthermore, all referenced methods used soft constraints to incorporate the feature/landmark correspondences, which are not capable of guaranteeing a maximal mismatch of corresponding features/points. The latter aspect was overcome by Papenberg et al., who – as an extension of [7, 9] – developed an approach for combination of landmark- and intensity-based registration, which even allows for individual tolerances for each landmark [23]. They, however, did neither integrate automatic landmark detection into the registration process nor addressed registration of lung CT data.

Here, we introduce a novel combination of variational nonlinear registration and automatically detected landmarks that is applied to pulmonary CT scan pairs. As there might be some misdetections of features and the accuracy of the

algorithm is limited by the voxel sizes, we restrict our model to an upper bound for the maximal landmark distance but allow for small mismatches. The integration of the feature-based registration is intended to stabilize the registration and improve robustness in presence of noise or reconstruction artifacts.

The remainder of the paper is organized as follows: Section 2 describes the methodical aspects of our approach. The main ingredients are variational image registration (Sect. 2.1), the integration of the landmark correspondences into the registration (Sect. 2.2), and automatic landmark detection (Sect. 2.3). The conducted experiments are detailed and evaluated in Section 3. Section 3.1 explains the used data and evaluation criteria; Section 3.2 contains the obtained registration results. In Section 4, these results are discussed.

2 Methods

2.1 Variational Image Registration

The aim of image registration is to find a plausible transformation $y: \mathbb{R}^d \rightarrow \mathbb{R}^d$ such that for a given template image $\mathcal{T}: \Omega_{\mathcal{T}} \rightarrow \mathbb{R}$ the transformed image $\mathcal{T}(y)$ becomes similar to a given reference image $\mathcal{R}: \Omega_{\mathcal{R}} \rightarrow \mathbb{R}$. The dimension of the image data is denoted by $d \in \mathbb{N}$ and $\Omega_{\mathcal{T}}, \Omega_{\mathcal{R}} \subset \mathbb{R}^d$ are the considered domains. We are handling this task by solving an unconstrained optimization problem. The objective function consists of several terms that are explained step by step. The basic model is equal to the one proposed by Riihaak et al. [25]

The similarity of two images is determined by the distance measure. We select a variant of the Normalized Gradient Fields (NGF) [10] distance measure which is well-suited for proper alignment of edges represented e. g. by vessels in the lung CT data [25]:

$$\mathcal{D}(\mathcal{T}(y), \mathcal{R}) := \int_{\Omega} 1 - \frac{\langle \nabla \mathcal{T}(y(x)), \nabla \mathcal{R}(x) \rangle_{\eta}^2}{\|\nabla \mathcal{T}(y(x))\|_{\eta}^2 \|\nabla \mathcal{R}(x)\|_{\eta}^2} dx, \quad (1)$$

with $\langle a, b \rangle_{\eta} := \eta^2 + \sum_{i=1}^d a_i b_i$ and $\|a\|_{\eta}^2 := \langle a, a \rangle_{\eta}$. The edge parameter $\eta \in \mathbb{R}$ is important to control the influence of noise in the data. We fixed $\eta = 100$ for all experiments. A major advantage of NGF is its independence of absolute intensity differences between corresponding areas in template and reference image as it was designed specifically for multi-modal image registration. This feature pays off especially in registration of images acquired during different breathing phases. Here, intensity differences occur due to altered density of lung tissue and hence changed absorption of X-rays during acquisition of CT data.

A regularizing functional guides the solution towards plausible solutions. With the definition of a kernel function y^{kernel} it is possible to avoid a penalization of reasonable transformations. We employ curvature regularization which was introduced in [8]:

$$\mathcal{S}(y) := \frac{1}{2} \sum_{i=1}^d \int_{\Omega} (\Delta(y_i(x) - y_i^{\text{kernel}}(x)))^2 dx. \quad (2)$$

It favors smooth transformations, which is very important when adding landmark information into registration [17]. Furthermore its energy is similar to the energy that is minimized during a landmark-based Thin-Plate-Spline (TPS) registration [18]. The TPS pre-registration maps the automatically detected reference landmarks onto the template landmarks, cf. section 2.2. We consider this TPS warp as plausible deformation and choose $y^{\text{kern}} = y^{\text{TPS}}$. The modeled smooth deformation is justifiable because sliding motion of the rib cage is eliminated by masking the images with a proper segmentation [25]. Lung segmentations were generated with the method of Lassen et al. [16].

To achieve a proper global alignment of the lungs and their boundaries we incorporate a lung mask penalty $\mathcal{B}(y)$ [24]. In terms of our segmentation masks it equals a sum of squared differences over all voxels. Alternatively it is defined for the binary functions $b_{\mathcal{R}}: \Omega_{\mathcal{R}} \rightarrow \{0, 1\}$ and $b_{\mathcal{T}}: \Omega_{\mathcal{T}} \rightarrow \{0, 1\}$ that equal one for positions inside the lungs and zero otherwise:

$$\mathcal{B}(y) := \frac{1}{2} \int_{\Omega_{\mathcal{R}}} (b_{\mathcal{T}}(y(x)) - b_{\mathcal{R}}(x))^2 dx . \quad (3)$$

Although the curvature regularization encourages smooth transformations there is no guarantee that locally extreme volume changes and foldings of the grid are avoided. We therefore add volume regularization to prevent singularities [24]:

$$\mathcal{V}(y) := \int_{\Omega_{\mathcal{R}}} \psi(\det \nabla y(x)) dx , \quad (4)$$

$$\text{with } \psi: \mathbb{R} \rightarrow \mathbb{R} \cup \{\infty\}, \quad \psi(t) := \begin{cases} \frac{(t-1)^2}{t}, & t > 0, \\ \infty, & t \leq 0. \end{cases} \quad (5)$$

Now we explain how the landmark information is combined with the intensity-based registration model.

2.2 Landmark integration

In the given context, landmarks are usually understood as characteristic points of the image domain and, consequently, landmark correspondences as point correspondences. The reference landmarks are denoted as $r_j \in \mathbb{R}^d$ and the template landmarks as $t_j \in \mathbb{R}^d$, $j = 1, 2, \dots, L$. We use landmarks to establish a Thin-Plate-Spline solution, which satisfies the landmark conditions:

$$y^{\text{TPS}}(r_j) = t_j, \quad \text{for all } j \in \{1, 2, \dots, L\} . \quad (6)$$

The TPS solution serves on the one hand as pre-registration and on the other hand as kernel transformation for the regularizer. The nonlinear registration might nevertheless negatively affect the successful landmark registration. We want to maintain the correspondences within a small tolerance and employ a log barrier method to restrict the transformation to a maximal displacement of

the transformed reference landmarks by $a' \in \mathbb{R}^+$ millimeters. The squared euclidean distance of the j -th transformed reference landmark to the corresponding template landmark is calculated and denoted by $f_j(y)$:

$$f_j(y) := \|y(r_j) - t_j\|_2^2, \quad j = 1, 2, \dots, L. \quad (7)$$

The log barrier penalty $\mathcal{P}(y)$ is based on all $f_j(y)$ and $a := (a')^2$:

$$\mathcal{P}(y) := - \sum_{j=1}^L \log \left(1 - \frac{f_j(y)}{a} \right). \quad (8)$$

If any $f_j(y) \geq a$ and hence $x = 1 - f_j(y)/a \leq 0$ we set $\log(x) = -\infty$. This way we ensure $\mathcal{P}(y) \rightarrow \infty$ if any $f_j(y) \rightarrow a$.

The sought transformation y is computed by solving an unconstrained optimization problem which equals a minimization of the following joint functional:

$$\mathcal{J}(y) := \mathcal{D}(\mathcal{T}(y), \mathcal{R}) + \alpha \mathcal{S}(y) + \beta \mathcal{B}(y) + \gamma \mathcal{V}(y) + \delta \mathcal{P}(y) \stackrel{!}{=} \min. \quad (9)$$

The four parameters $\alpha, \beta, \gamma, \delta \in \mathbb{R}^+$ allow for an individual weighting of the corresponding terms. The parameters were chosen empirically as $\alpha = 5, \beta = 1, \gamma = 10^{-3}, \delta = 250$ and $a = 5$ for all experiments.

A solution of (9) is obtained in a Discretize-then-Optimize scheme using multilevel representations of the data [18]. By solving the problem from coarse to fine resolution, the risk of getting stuck in local minima during optimization is reduced and the multilevel approach acts as an additional regularizer. For numerical optimization of the discretized objective functional J the L-BFGS quasi-Newton method combined with Armijo line search and conjugate gradients solver was used [21]. If the initial deformation is feasible the line search guarantees feasibility during further optimization despite of difficulties arising from the terms \mathcal{P} and \mathcal{V} .

2.3 Automated Detection of Landmark Correspondences

The automated detection of landmark correspondences $(r_j, t_j), j = 1, 2, \dots, L$, in $\Omega_{\mathcal{R}}$ and $\Omega_{\mathcal{T}}$ is based on [28]. The applied algorithm consists of two phases: identification of appropriate landmark candidates $r_j^{\text{cand}}, j = 1, 2, \dots, L' \gg L$, in $\Omega_{\mathcal{R}}$ and transferring them to $\Omega_{\mathcal{T}}$.

For identification of the r_j^{cand} , we apply the so-called Foerstner3D operator to \mathcal{R} . Retaining the original notation of [11], the operator is defined as

$$\text{Foerstner3D} := \frac{1}{\text{trace}((K_{\sigma} * (\nabla \mathcal{R} \nabla \mathcal{R}^T))^{-1})}, \quad (10)$$

with K_{σ} being a Gaussian kernel of variance σ (here: $\sigma = 1$) and the structure tensor $\nabla \mathcal{R} \nabla \mathcal{R}^T : \Omega_{\mathcal{R}} \rightarrow \mathbb{R}^{d \times d}$. Voxels with high operator answers are interpreted as suitable candidates, i.e., the lung voxel with the highest Foerstner3D

value is selected as first landmark candidate. Additional lung voxels with high operator answers are then continuously added to the candidate set (until the pre-defined maximum number L' of candidates), with a minimum Euclidean distance being postulated to be kept between the candidates to provide an approximately equal distribution of the landmarks within the lungs [19] (original distance: 50 voxel; if no voxels with high operator values are available for this value, the distance is iteratively decreased).

Similar to [28], we use a cross correlation (CC)-based blockmatching strategy for transferring the candidates r_j to $\Omega_{\mathcal{T}}$. In [28], a two-step approach was suggested: For each r_j , a first block matching was performed using the original intensity values of \mathcal{R} and \mathcal{T} , followed by a block matching based on the answers of the differential operator applied for identification of the r_j . To detect and reject implausible transfers, the results of both runs were compared. This approach has been reported to be robust especially for automatic landmark detection in 4D-CT data sets [6, 28]; however, for, e.g., landmark detection in normal and low dose CT scan pairs, we observed only a small fraction of the detected landmark candidates to be classified as being reliably transferred by this approach.

In this work, we adopt the idea of learning a TPS transformation in parallel to the landmark candidate transfer, as originally proposed by Murphy et al. [19]: Starting with the corner points of the bounding boxes of the lung masks and a small set of candidates r_j that are located in the upper region of the lungs and feature high correlation values for the intensity-based block matching (correlation coefficient > 0.7), we test the robustness of the block matching results for the remaining candidates on a landmark-by-landmark basis by comparing the block matched landmark position and its location as suggested by the TPS warp. If both positions were within a three-voxel agreement, the correspondence $(r_j^{\text{cand}}, y^{\text{TPS}}(r_j^{\text{cand}}))$ is used as additional supporting point of the (recalculated) TPS warp; otherwise, the point matching is interpreted as not being reliable and rejected. After testing all L' landmark candidates, the resulting TPS transformation is – in the sense of a final correction step – again applied to the rejected landmark candidates $r_j^{\text{cand, rej}}$. Assuming the TPS as being roughly correct on a global scale, a local intensity- and CC-based block matching is performed in the proximity of $y^{\text{TPS}}(r_j^{\text{cand, rej}})$ and the resulting correspondence added to the final landmark correspondence set in the case of a high correlation value.

3 Experiments

3.1 Data and Evaluation

We used twenty publicly available data sets provided by the DIR-Lab [2, 4, 5] for evaluation purposes. The data sets 1 to 10 are pulmonary 4D-CT data sets, for which we used the scan during maximal expiration as template and the maximal inspiration scan as reference image. The data sets 11 to 20 originate from the COPDgene study. Here, we employed the inspiration scan as template and the expiration scan as reference image.

Table 1. Number of automatically detected landmarks located in the left lung (L_{left}) respectively in the right lung (L_{right}) and minimal pairwise euclidean distance in reference and template domain (values given in mm).

Case	L_{left}	L_{right}	Min. distance in $\Omega_{\mathcal{R}}$	Min. distance in $\Omega_{\mathcal{T}}$
1	122	251	9.03	6.10
2	151	224	12.20	10.52
3	163	180	10.06	8.26
4	73	126	9.04	7.11
5	112	110	9.07	7.58
6	41	96	11.00	8.44
7	55	118	11.00	8.66
8	77	103	14.01	12.14
9	65	122	8.04	5.79
10	84	113	10.11	7.81
11	186	173	13.01	9.72
12	84	179	10.02	5.66
13	231	384	13.02	6.07
14	73	148	9.03	7.10
15	94	245	10.02	6.63
16	262	306	11.01	8.48
17	145	337	11.04	7.55
18	199	229	10.04	10.04
19	268	298	10.02	8.95
20	92	168	12.00	10.04

Each data set contains 300 landmark pairs that were manually annotated by medical experts. These landmarks were used for evaluation of registration accuracy but not during the registration process. Computing the distance of landmarks after registration is a common procedure for evaluation, cf. e. g. [20]. That is why the statistics of landmark errors are widely published and can be compared to the literature, e. g. [3, 12, 25, 26]. We directly compute the euclidean distances between transformed reference and corresponding template landmark for all 300 landmarks and compare means and standard deviations.

In detail, we compared the proposed method, called LMP (registration with LandMark Penalty), our former approach without landmark usage (NLR abbreviation for NonLinear Registration) [25], the TPS solution and the gsyn method [1, 27], which is the best ranked algorithm of the EMPIRE10 benchmark and part of the open-source ANTS library. According to [27], the images were pre-processed before we applied the gsyn algorithm. First they were masked with the same lung segmentations that we used in our methods. As second step the data was normalized to the interval $[0,1]$. An affine pre-registration of the lung masks preceded the registration of the pre-processed data; all parameters were chosen to be equal to the ones reported in [27].

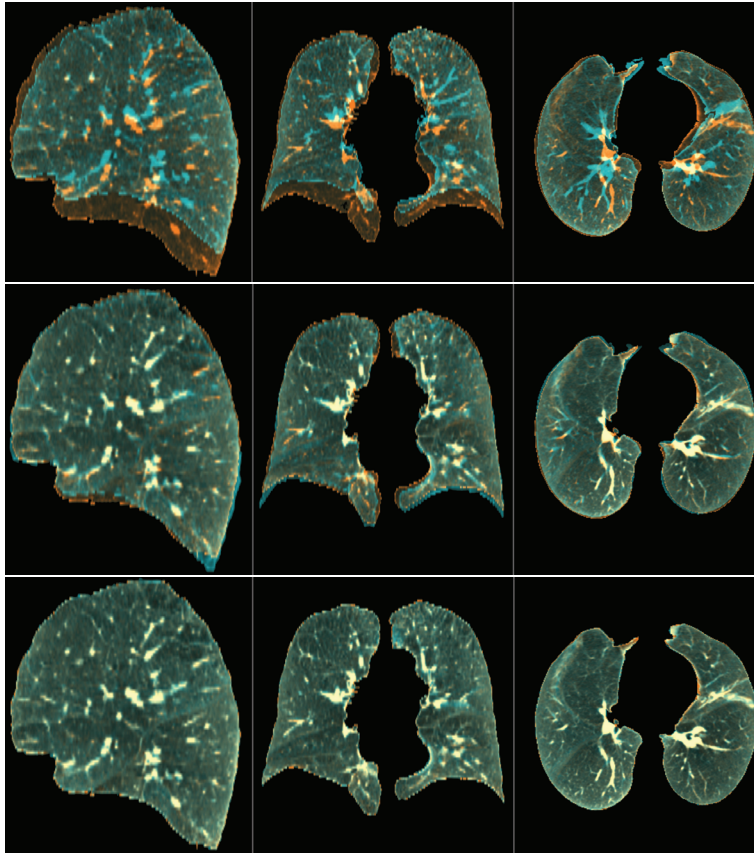


Fig. 1. Overlay of reference (orange) and (transformed) template (blue) image in orthogonal views of the 8th case. Top row: Initial situation, middle row: Result of TPS registration, bottom row: Result of LMP registration. Correctly aligned structures appear gray, particularly vessels appear white.

3.2 Results

Some properties of the automatically detected landmarks are given in table 1. On average the right lung contains more landmarks than the left one which is plausible because of the different volumes. Figure 1 shows registration results as an overlay of reference and transformed template image. Visual inspection of the middle row indicates a good alignment of large vessels and lung boundaries by the pure landmark-based TPS solution. This serves as an excellent starting point for the subsequent optimization by LMP (bottom row). A similar situation is depicted in Figure 2 where the movement in the original images is obviously large and makes the registration challenging. This is a property of all COPDgene data sets (cases 11 to 20), cf. second column of Table 2.

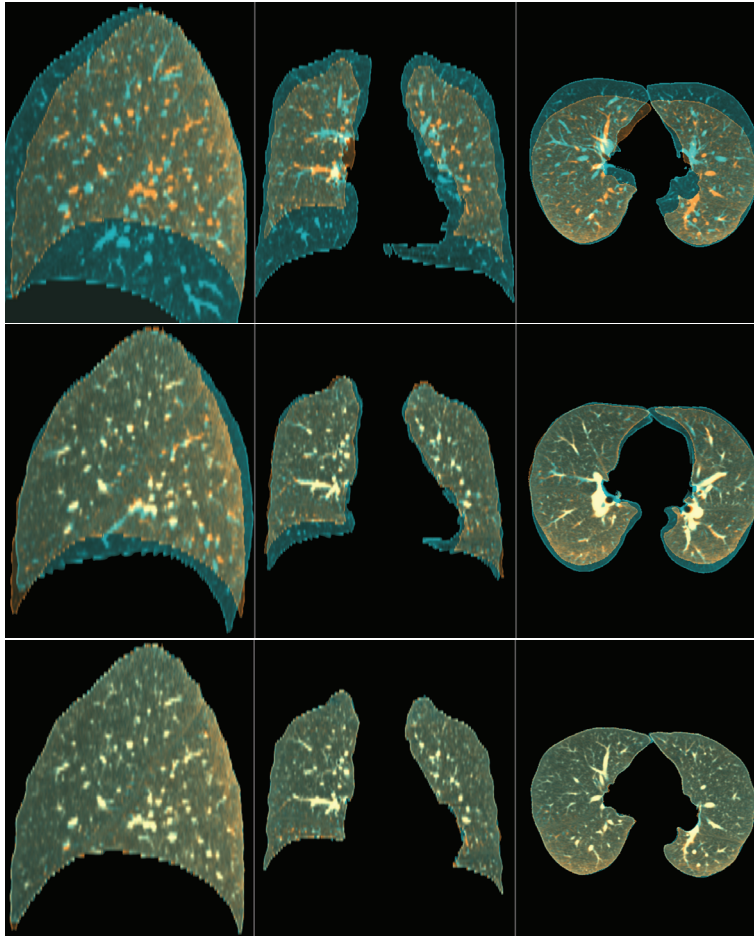


Fig. 2. Overlay of reference (orange) and (transformed) template (blue) image in orthogonal views of the 18th case (b). Top row: Initial situation, middle row: Result of TPS registration, bottom row: Result of LMP registration. Correctly aligned structures appear gray; in particular large vessels appear white.

The comparison of the tested methods with respect to landmark errors is given in Table 2. The results for the NLR method by Rühaak et. al [25] slightly differ from the published ones because we do not move the transformed reference landmark to the next voxel center. Instead, we directly calculate the euclidean distances in world coordinates. Concerning the first ten cases, our proposed approach LMP shows good results with a mean error being in the order of the inter-observer variability of the landmarks and close to the axial resolution, cf. [2, 5]. The small standard deviation additionally increases reliability, which is important for clinical applications. One can easily see that by integration of the landmarks no benefit could be gained in comparison to NLR. Nevertheless, it

Table 2. Comparison of means (standard deviations) of distances of 300 manually annotated landmark pairs before and after registration of end-inspiration and end-expiration phases of the DIR-Lab data. Values given in mm.

Case	initial	Observer error	NLR	gsyn	our method	TPS
1	3.89 (2.78)	0.85 (1.24)	0.98 (0.49)	1.00 (0.49)	0.95 (0.51)	0.99 (0.78)
2	4.34 (3.90)	0.70 (0.99)	0.96 (0.46)	1.00 (0.50)	0.94 (0.47)	0.97 (0.64)
3	6.94 (4.05)	0.77 (1.01)	1.09 (0.62)	1.13 (0.61)	1.07 (0.64)	1.27 (0.90)
4	9.83 (4.86)	1.13 (1.27)	1.36 (0.96)	1.37 (0.96)	1.35 (0.96)	1.93 (1.33)
5	7.48 (5.51)	0.92 (1.16)	1.25 (1.23)	1.34 (1.24)	1.26 (1.24)	1.90 (1.45)
6	10.89 (6.97)	0.97 (1.38)	1.11 (0.66)	1.11 (0.66)	1.10 (0.67)	1.94 (1.40)
7	11.03 (7.43)	0.81 (1.32)	1.04 (0.63)	1.11 (0.80)	1.05 (0.63)	2.02 (1.32)
8	15.00 (9.01)	1.03 (2.19)	1.14 (0.93)	1.24 (1.44)	1.13 (0.90)	2.11 (1.37)
9	7.92 (3.98)	0.75 (1.09)	1.07 (0.65)	1.12 (0.73)	1.07 (0.65)	1.83 (1.03)
10	7.30 (6.35)	0.86 (1.45)	1.03 (0.64)	1.05 (0.63)	1.03 (0.65)	1.78 (1.44)
Avg 1-10	8.46 (5.48)	0.88 (1.31)	1.10 (0.73)	1.15 (0.81)	1.10 (0.73)	1.67 (1.17)
11	26.33 (11.44)	0.65 (0.73)	1.39 (1.40)	1.21 (1.36)	1.26 (1.23)	3.69 (3.79)
12	21.79 (6.47)	1.06 (1.51)	2.36 (2.79)	3.01 (4.46)	2.02 (2.29)	4.10 (3.60)
13	12.64 (6.40)	0.58 (0.87)	1.18 (0.81)	1.24 (1.08)	1.14 (0.70)	1.56 (1.07)
14	29.58 (12.95)	0.71 (0.96)	1.57 (1.39)	1.38 (1.14)	1.62 (1.60)	4.39 (3.89)
15	30.08 (13.36)	0.65 (0.87)	1.44 (1.14)	1.31 (1.19)	1.47 (1.26)	3.63 (3.31)
16	28.46 (9.17)	1.06 (2.38)	2.08 (2.92)	1.49 (2.25)	1.38 (1.46)	2.69 (2.94)
17	21.60 (7.74)	0.65 (0.78)	1.18 (1.13)	1.24 (1.24)	1.22 (1.30)	2.25 (2.18)
18	26.46 (13.24)	0.96 (3.07)	1.65 (1.98)	2.09 (3.32)	1.63 (2.16)	3.47 (3.76)
19	14.86 (9.82)	1.01 (2.54)	1.13 (1.09)	1.18 (1.25)	1.12 (1.14)	2.20 (2.34)
20	21.81 (10.51)	0.87 (1.65)	1.44 (1.23)	1.63 (2.05)	1.45 (1.31)	4.00 (3.16)
Avg 11-20	23.36 (10.11)	0.82 (1.54)	1.54 (1.59)	1.58 (1.93)	1.43 (1.45)	3.20 (3.00)
Avg 1-20	15.91 (7.80)	0.85 (1.42)	1.32 (1.16)	1.36 (1.37)	1.26 (1.09)	2.44 (2.09)

does not interfere the variational registration. The gsyn method performs almost as good as NLR/LMP and the TPS method is according to the landmark error on manually annotated landmarks the worst one. However, TPS works surprisingly well although it does not use intensity information. Especially in the first two cases almost no difference to any of the other methods is visible. On data sets 11 to 20, a difference between NLR and LMP is visible. On average, the model that integrates the landmark knowledge performs better than NLR. The gsyn method performs well – as expected because gsyn is ranked first in the EMPIRE10 challenge – but on average the mean landmark error is 10 % larger than the value of our proposed method. The TPS method, which was investigated as proof of concept, is not as accurate as the other three test methods but, nevertheless, the mean landmark error is dramatically decreased compared to the initial values.

Unfortunately there are no published results for the registration of the DIR-Lab COPDgene data yet which makes a comparison impossible. In contrast a lot of groups tested their methods on the DIR-Lab 4D datasets and we will briefly report on their results. Each result has the format mean±standard deviation. Heinrich et al. achieved 1.43 ± 1.30 mm [12] and Schmidt-Richberg et al. attained 1.35 ± 0.90 mm [26]. The DIR-Lab group presented two approaches

that use information of intermediate scans for registration [2]. They evaluated the registrations on larger sets of landmarks containing the 300 publicly available ones. 4DLTM achieves on average 1.35 ± 1.47 mm and CPP 1.56 ± 1.57 mm. Their recently published LFC method [3] had on average 1.03 ± 1.12 mm landmark error. All their evaluations were evaluated in a move to voxel center manner meaning that the transformed reference landmark was moved towards the next voxel center as the template landmark is always localized on the grid. After this rounding procedure, the landmark distances were calculated. If we calculate the distances the same way LMP achieves an average error of 0.95 ± 1.07 mm.

4 Discussion

We have presented a method for registration of lung CT scans that competes successfully with several state-of-the-art algorithms on the 20 DIR-Lab data sets. The integration of additional knowledge represented by automatically detected landmarks makes the nonlinear registration very robust and provides an excellent starting point. Additionally, the landmark penalty guarantees that successfully registered automatically detected landmarks maintain a distance below a user-defined threshold. We could show that this is especially useful on the more difficult COPDgene data sets.

References

1. Avants, B.B., Epstein, C.L., Grossman, M., et al.: Symmetric Diffeomorphic Image Registration with Cross-Correlation: Evaluating Automated Labeling of Elderly and Neurodegenerative Brain. *Medical Image Analysis* 12(1), 26–41 (2008)
2. Castillo, E., Castillo, R., Martinez, J., et al.: Four-dimensional deformable image registration using trajectory modeling. *Physics in Medicine and Biology* 55(1), 305–327 (2010)
3. Castillo, E., Castillo, R., White, B., et al.: Least median of squares filtering of locally optimal point matches for compressible flow image registration. *Physics in Medicine and Biology* 57(15), 4827–4833 (2012)
4. Castillo, R., Castillo, E., Fuentes, D., et al.: A Reference Dataset for Deformable Image Registration Spatial Accuracy Evaluation using the COPDgene Study Archive. *Physics in Medicine and Biology* 58(9), 2861 (2013)
5. Castillo, R., Castillo, E., Guerra, R., et al.: A framework for evaluation of deformable image registration spatial accuracy using large landmark point sets. *Physics in Medicine and Biology* 54(7), 1849–1870 (2009)
6. Ehrhardt, J., Werner, R., Schmidt-Richberg, A., et al.: Automatic Landmark Detection and Non-linear Landmark- and Surface-based Registration of Lung CT Images. In: *Medical Image Analysis for the Clinic - A Grand Challenge* (2010)
7. Fischer, B., Modersitzki, J.: Combining landmark and intensity driven registrations. *Proceedings in Applied Mathematics and Mechanics* 3(1), 32–35 (2003)
8. Fischer, B., Modersitzki, J.: Curvature Based Image Registration. *Journal of Mathematical Imaging and Vision* 18, 81–85 (2003)
9. Haber, E., Heldmann, S., Modersitzki, J.: A Scale-Space Approach to Landmark Constrained Image Registration. In: *2nd Intern. Conference on Scale Space Methods and Variational Methods in Computer Vision*. pp. 1–12. Springer LNCS (2009)

10. Haber, E., Modersitzki, J.: Intensity Gradient Based Registration and Fusion of Multi-modal Images. *Methods of Information in Medicine* 46(3), 292–299 (2007)
11. Hartkens, T., Rohr, K., Stiehl, H.S.: Evaluation of 3D Operators for the Detection of Anatomical Point Landmarks in MR and CT Images. *Computer Vision and Image Understanding* 86, 118–136 (2002)
12. Heinrich, M., Jenkinson, M., Brady, S., et al.: MRF-Based Deformable Registration and Ventilation Estimation of Lung CT. *IEEE Transactions on Medical Imaging* (accepted) (2013)
13. Hellier, P., Barillot, C.: Coupling Dense and Landmark-Based Approaches for Non-rigid Registration. *IEEE Transactions on Medical Imaging* 22(2), 217–227 (2003)
14. Johnson, H.J., Christensen, G.E.: Consistent Landmark and Intensity-Based Image Registration. *IEEE Transactions on Medical Imaging* 21(5), 450–461 (2002)
15. Kybic, J., Unser, M.: Fast Parametric Elastic Image Registration. *IEEE Transactions on Image Processing* 12(11), 1427–1442 (2003)
16. Lassen, B., Kuhnigk, J.M., Schmidt, M., et al.: Lung and Lung Lobe Segmentation Methods at Fraunhofer MEVIS. In: 4th International Workshop on Pulmonary Image Analysis. pp. 185–199 (2011)
17. Modersitzki, J.: Numerical Methods for Image Registration. Oxford University Press, New York (2004)
18. Modersitzki, J.: FAIR: Flexible Algorithms for Image Registration. SIAM, Philadelphia (2009)
19. Murphy, K., van Ginneken, B., Klein, S., et al.: Semi-automatic Construction of Reference Standards for Evaluation of Image Registration. *Medical Image Analysis* 15(1), 71–84 (2011)
20. Murphy, K., van Ginneken, B., Reinhardt, J.M., et al.: Evaluation of Registration Methods on Thoracic CT: the EMPIRE10 Challenge. *IEEE Transactions on Medical Imaging* 30(11), 1901–1920 (2011)
21. Nocedal, J., Wright, S.J.: Numerical Optimization. Springer, New York (2006)
22. Papademetris, X., Jackowski, A.P., Schultz, R.T., et al.: Integrated Intensity and Point-Feature Nonrigid Registration. In: Medical Image Computing and Computer-Assisted Intervention—MICCAI 2004. pp. 763–770. Springer (2004)
23. Papenberg, N., Olesch, J., Lange, T., et al.: Landmark Constrained Non-parametric Image Registration with Isotropic Tolerances. In: Bildverarbeitung für die Medizin. pp. 122–126. Informatik aktuell, Springer (2009)
24. Rühaak, J., Heldmann, S., Fischer, B.: Improving Lung Registration by Incorporating Anatomical Knowledge: A Variational Approach. In: 4th International MICCAI Workshop on Pulmonary Image Analysis (2011)
25. Rühaak, J., Heldmann, S., Kipshagen, T., et al.: Highly Accurate Fast Lung CT Registration. In: SPIE Medical Imaging 2013: Image Processing (2013)
26. Schmidt-Richberg, A., Werner, R., Ehrhardt, J., et al.: Landmark-driven Parameter Optimization for Non-linear Image Registration. *SPIE Medical Imaging* 2011 7962, 0T1–0T8 (2011)
27. Song, G., Tustison, N., Avants, B., et al.: Lung CT Image Registration Using Diffeomorphic Transformation Models (2010), http://empire10.isi.uu.nl/pdf/article_picslgsyn.pdf, accessed on 11.06.2013
28. Werner, R., Duscha, C., Schmidt-Richberg, A., et al.: Assessing Accuracy of Non-linear Registration in 4D Image Data using Automatically Detected Landmark Correspondences. In: SPIE Medical Imaging 2013: Image Processing. vol. 8669, pp. 1–9 (2013)